Overview of the Large Helical Device project

A. IIYOSHI, A. KOMORI, A. EJIRI, M. EMOTO, H. FUNABA,
M. GOTO, K. IDA, H. IDEI, S. INAGAKI, S. KADO, O. KANEKO,
K. KAWAHATA, T. KOBUCHI, S. KUBO, R. KUMAZAWA,
S. MASUZAKI, T. MINAMI, J. MIYAZAWA, T. MORISAKI,
S. MORITA, S. MURAKAMI, S. MUTO, T. MUTO, Y. NAGAYAMA,
Y. NAKAMURA, H. NAKANISHI, K. NARIHARA, K. NISHIMURA,
N. NODA, S. OHDACHI, N. OHYABU, Y. OKA, M. OSAKABE,
T. OZAKI, B.J. PETERSON, A. SAGARA, S. SAKAKIBARA,
R. SAKAMOTO, H. SASAO, M. SASAO, K. SATO, M. SATO, T. SEKI,
T. SHIMOZUMA, M. SHOJI, H. SUZUKI, Y. TAKEIRI, K. TANAKA,
K. TOI, T. TOKUZAWA, K. TSUMORI, K. TSUZUKI,
K.Y. WATANABE, T. WATARI, H. YAMADA, I. YAMADA,
S. YAMAGUCHI, M. YOKOYAMA, R. AKIYAMA, H. CHIKARAISHI,
K. HABA, S. HAMAGUCHI, M. IIMA, S. IMAGAWA, N. INOUE,
K. IWAMOTO, S. KITAGAWA, J. KODAIRA, Y. KUBOTA,
R. MAEKAWA, T. MITO, T. NAGASAKA, A. NISHIMURA,
C. TAKAHASHI, K. TAKAHATA, Y. TAKITA, H. TAMURA,
T. TSUZUKI, S. YAMADA, N. YANAGI, K. YAMAUCHI, H. YONEZU,
Y. HAMADA, K. MATSUOKA, K. MURAI, K. OHKUBO, I. OHTAKE,
M. OKAMOTO, S. SATOH, T. SATOW, S. SUDO, S. TANAHASHI,
K. YAMAZAKI, M. FUJIWARA, O. MOTOJIMA

National Institute for Fusion Science,
Toki, Japan

Abstract

OVERVIEW OF THE LARGE HELICAL DEVICE PROJECT.

The Large Helical Device (LHD) has successfully started running plasma confinement experiments after a long construction period of eight years. During the construction and machine commissioning phases, a variety of milestones were attained in fusion engineering which successfully led to the first operation, and the first plasma was ignited on 31 March 1998. Two experimental campaigns are planned in 1998. In the first campaign, the magnetic flux mapping clearly demonstrated a nested structure of magnetic surfaces. The first plasma experiments were conducted with second harmonic 84 and 82.6 GHz ECH at a heating power input of 0.35 MW. The magnetic field was set at 1.5 T in these campaigns so as to accumulate operational experience with the superconducting coils. In the second campaign, auxiliary heating with NBI at 3 MW has been carried out. Averaged electron densities of up to 6×10^{19} m^{-3}, central temperatures ranging from 1.4

to 1.5 keV and stored energies of up to 0.22 MJ have been attained despite the fact that the impurity level has not yet been minimized. The obtained scarling of energy confinement time has been found to be consistent with the ISS95 scaling law with some enhancement.

1. Introduction

The Large Helical Device (LHD) offers a great opportunity to study currentless plasmas in the heliotron configuration. LHD is a large heliotron with a major radius R of 3.9 m and a minor radius a of 0.65 m [1-4]. Full steady state operation is expected, using superconducting coils in addition to a full helical divertor. Steady state plasma operation, essential to magnetic fusion reactors, is an inherent advantage of heliotrons over tokamaks and can be realized with the full helical divertor because it removes heat flux from the core plasma and controls impurity recycling. However, since the closed full helical divertor will not be ready in the near future, we plan to use a local island divertor (LID) for the LHD edge plasma control [5, 6]. The LID is a closed divertor that uses an m/n = 1/1 island. The technical ease of hydrogen pumping is the advantage of the LID over the closed full helical divertor because hydrogen recycling is toroidally localized [5, 6].

The eight year construction phase has led to the successful engineering commissioning of the device. Figure 1 shows a picture of LHD taken in the second campaign. The basic physics objectives are [1]: (1) to produce high $n\tau T$ currentless plasmas and study transport issues to obtain basic data which can be extrapolated to reactor grade plasmas; (2) to achieve high-β plasmas with $\langle\beta\rangle > 5\%$ and to study the related physics; (3) to install a divertor and obtain basic data for steady state operation; (4) to study the behaviour of high energy particles in the heliotron magnetic field and conduct simulation experiments of alpha particles in reactor plasmas; and (5) to promote

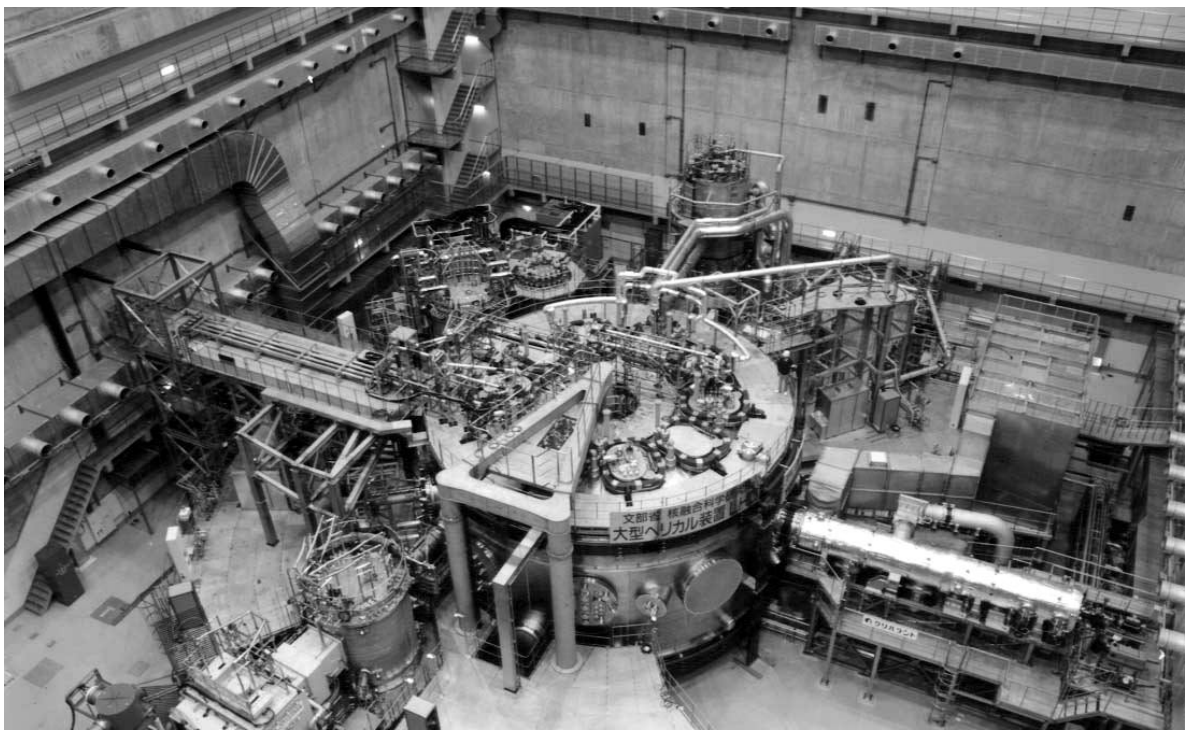

Figure 1. Photograph of LHD taken during the second campaign

complementary studies for tokamak plasmas to increase understanding of magnetically confined toroidal plasmas. Engineering R&D experience has also contributed to advances in fusion technology. LHD employs a pair of ℓ/m = 2/10 helical coils (liquid helium pool cooled), three sets of poloidal coils (supercritical helium forced flow cooled) and nine pairs of bus lines (two fluid helium forced flow cooled). The mass at the cryogenic temperature of 4.4 K is 822 t. The transition to the superconductiong state has been achieved after four weeks' cooling of the coils.

Initial plasma experiments have started with second harmonic 82.6 and 84 GHz ECH of 0.35 MW at 1.5 T. NBI of 3 MW with negative ion sources, optimized for a low energy of 100 keV, has been applied in the second campaign. This article is intended to present an overview of the LHD project, including the construction procedure, the associated technology R&D activities, the plasma confinement experiments in the first campaign, the updated results from auxiliary heating experiments with NBI in the second campaign, future plans and so on.

2. Advanced technology

The specifications of LHD are shown in Table 1. Notice that we have two operational regimes for LHD. In Phase I the helical magnetic field is set at 3 T, whereas the field will be increased to 4 T in Phase II.

Along with the design and construction efforts, a tremendous amount of knowledge has been obtained in the areas of cryogenic engineering, plasma facing components and so on. This article is intended to summarize the main results in areas of cryogenic engineering, plasma heating devices and diagnostics. The detailed technology R&D is presented elsewhere [7].

Table 1. Specifications of LHD

Items	Phase I [II]
Major radius (R)	3.9 m
Minor radius (a)	0.65 m
Plasma volume (V_p)	30 m^3
Coil minor radius (a_c)	0.975 m
Magnetic field (B_t)	3 [4] T
Magnetic energy	0.9 [1.6] GJ
Heating power	
ECH	10 MW
NBI	15 [20] MW
ICRF	3–12 MW
Target plasma	
T_i	> 10 keV
$n\,\tau_E\,T_i$	> 10^{20} $keVm^{-3}$ s
β	> 5%

2.1. R&D of superconducting coils

The specifications of the coil sets are listed in Table 2. The poloidal coil system includes three sets - inner vertical (IV), inner shaping (IS) and outer vertical (OV) coils - all of which are superconducting. The bracketed numbers in Table 2 represent the parameters in Phase II.

Table 2. Major parameters of superconducting coils

Items	Helical coil	IV coil	IS coil	OV coil
Major Radius (m)	3.90	1.80	2.82	5.55
Weight per coil (ton)	120	16	25	45
Magnetic stored energy (GJ)	0.92 [1.64]	0.16	0.22	0.61
Coil current density (A/mm^2)	40 [53]	29.8	31.5	33.0
Magnetomotive force (MA)	5.85 [7.8]	5.0	-4.5	-4.5
Number of turns	150×3	240	208	144
Conductor length (km)	36	2.7	3.7	5.0
Voltage to earth (kV)	±1.18 [±1.57]	±1.62	±1.75	±1.87
Cooling method	Pool-cooled	Forced flow	←	←
Number of flow paths	20	16	←	←
Length of a flow path (m)	3.9	170	230	314
Coil temperature (K)	4.4 [1.8]	4.5 – 4.8	←	←
Hoop force (MN)	356	262	116	263
Vertical force (MN)	240	-60.2	95.6	72.2

For attaining highly accurate helical shaping and winding, we selected pool cooled medium size conductors for the helical coils. After many short sample tests [8], the final size was chosen to be 12.5 mm × 18.0 mm, and the nominal current is 13.0 kA at 4.4 K for the 3 T operation. The main stabilizer is made of pure aluminium. The conductor size was optimized not only for the mechanical flexibility for winding but also for high cryogenic stability. In order to reduce the magnetoresistance caused by the Hall current, the aluminium structure is clad with Cu-2%Ni while maintaining a smooth current transfer from the superconducting strands [9].

Cable-in-conduit conductors are used for the poloidal coils because of their high strength and rigidity against large electromagnetic forces. The void fraction was optimized from the viewpoint of strand movement and interstrand coupling losses. The strand surface is uncoated to maintain current redistribution and heat transfer to the coolant. We confirmed with a mock-up coil that the bare strands provide a high stability margin during steady state operation [10].

A superconducting flexible busline was developed for the current feeding system. An aluminium stabilized compacted strand cable was developed to achieve full cryostability for 32 kA. A pair of conductors is pulled into the 50 m long coaxial corrugated tubes. We constructed a 20 m long full scale mock-up. Performance tests were carried out, and we confirmed that the minimum

propagating current is higher than 32.5 kA and that current up to 40 kA can flow without quenching [11].

2.2. R&D in cryogenic engineering

The cryogenic engineering R&D includes: (1) a winding device and technique for superconducting helical coils to achieve a high dimensional accuracy [12]; (2) a winding technique for cable-in-conduit conductors; (3) the materials and the welding technique for a thick (100 mm) structure of SUS 316 for cryogenic use [13]; (4) a new coil protection circuit with a fuse [14]; and (5) an advanced control system for the cryogenic system, using VME controllers and workstations [15].

2.3. R&D of plasma heating devices

Plasma heating devices using the ECH, NBI and ICRF techniques are employed in LHD experiments.

We use ECH for plasma production and heating with gyrotrons at the characteristic frequencies of 84, 82.6 and 168 GHz. The 168 GHz gyrotron is designed to be operated at steady state. The R&D results are that the output power of the 84 GHz gyrotron is 0.45 MW for 10.2 s and 0.5 MW for 2 s, and that of the 168 GHz gyrotron is 0.5 MW for 1 s. The ECH power is injected through two ports in the first and second campaigns, and two transmission lines are installed in each port. The elliptical Gaussian beam is focused on the equatorial plane and the focal point can be changed radially and toroidally.

Two negative ion based neutral beam injectors are the main heating devices, and are aligned for tangential injection in opposite directions (co- and counter-injection). Each neutral beam injector was designed for injecting a 7.5 MW hydrogen beam at an energy of 180 keV for 10 s by two ion sources. One of the two injectors was also designed to inject a 100 keV, 0.5 MW beam for up to 90 s. In the R&D, the extracted negative ion beam current reached 25 A, more than halfway to the goal value of 40 A, with a beam divergence of 10 mrad in the test ion source.

An ICRF heating system has been also developed. The 25-100 MHz variable high power cavity was developed for steady state ICRF heating with a total power of 3 MW, and two kinds of wave launchers were prepared for the second and third campaigns. These launchers include a 1 MW class half turn antenna for fast wave heating and a 0.5 MW class folded wave guide for ion Berstein wave heating.

2.4. Plasma vacuum vessel and density control

The plasma vacuum vessel is located inside the helical coils and is helically twisted. In order to maintain high accuracy in constructing the helical coils, it was decided that the plasma vacuum

vessel should be assembled after the installation of the helical coils. Thus the plasma vacuum vessel was divided into 140 parts. The joint welding was carried out after all of these parts were installed. Water cooling pipes were welded on the vessel surface facing the plasma.

Water cooled divertor plates will be installed at the divertor strike point areas after the second experimental campaign. Baffle plates are to be installed to form the closed full helical divertor, and a toroidal pump along four divertor legs will be installed near the divertor plates for density control. The carbon sheet pump [16] and membrane pump [17] have been evaluated for this purpose. The plasma vacuum vessel is to accommodate these pumps in a dumb-bell shaped cross-section.

2.5. R&D of heavy ion beam probe

A heavy ion beam probe has been designed for potential profile measurements in LHD [18]. Because of the large plasma and high magnetic field in LHD, a heavy ion beam, for example gold, needs to be accelerated as high as 6 MeV to penetrate the plasma. The beam should have a small energy spread, and hence a negative ion source of the plasma sputter type has been developed. Negative ions are accelerated in a tandem manner at first and are converted into positive ions through a stripping gas cell which is at the high voltage end. A test stand has been constructed to study the negative ion production, extraction, energy dispersion and charge stripping efficiency.

2.6. Overview of construction and assembly

The emphasis during the construction was on keeping the work quality high on the basis of the following principles: (1) technology innovations are encouraged; and (2) the National Institute for Fusion Science (NIFS) will be responsible for the final device performance, reducing the manufacturers' cost.

The detailed design work started in 1990 and parts construction in the factory started in 1991. Owing to the long lead time, the production of superconducting coils was initiated immediately from the production of superconducting wires. The on-site construction of LHD started in 1994 following the completion of the housing building. LHD construction was completed at the end of 1997.

The specifications and cross-section of the cryostat are shown in Fig. 2. Since the electromagnetic force is large, the helical coil conductors are packed into thick stainless steel cases (HC can) that are supported by 100 mm thick supporting structures. The assembly of the major components was carried out as follows: (1) assembly of the HC cans on a winding core; (2) winding of the helical-coil conductors in the cans; (3) assembly of the top covers on the HC cans; (4) assembly of the outer parts of the plasma vacuum vessel provisionally between the helical coils; (5) setting of the lower poloidal coils and the lower half of the supporting structure on the base plate of the cryostat; (6) installation of the whole assembly of helical coils on the lower half of the supporting structure; (7) installation of the upper half of the supporting structure and welding of the

<Supporting strucurse for coils>	
Thickness	100 mm
Weight	390 ton
Material	SUS316
Cooling channel	attached pipes
<Cryostat vessel and base>	
Diameter and height	13.5× 8.8 m
Volume	580 m^3
Weight (vessel / base)	350 / 200 ton
Material of vessel	SUS304
Material of base	manganese steel
Thickness of vessel	50 and 100 mm
Number of ports	95
<Cryogenic post>	
Load (cryogenic mass)	822 ton
Displacement by cooling	13 mm
Earthquake	0.3 G
Material	CFRP, SUS316
Heat input (to 4 / 80 K)	30 / 600 W

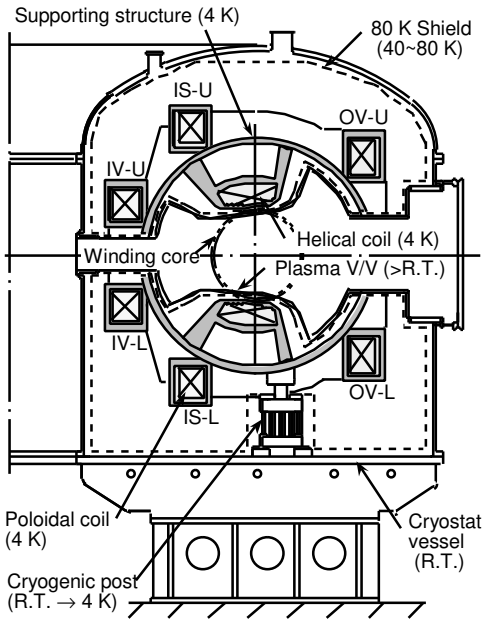

Figure 2. Specifications and cross-section of the cryostat.

whole assembly; (8) setting of the upper poloidal coils and adjustment of the whole coils; (9) removal of the winding core and assembly of the inner parts of the plasma vacuum vessel; and (10) assembly of the cryostat.

Quality control is important for a large system like LHD. We carried out various tests during both component and on-site construction periods, such as measurements of material properties, dimension tolerance checks, voltage ensuring tests and leak test. Furthermore, we performed several proof tests to ensure the result of the subsystems; for example, one of the IV coils was cooled down and excited up to the nominal current with a testing cryostat and test facilities at NIFS [19].

3. Commissioning

After machine assembly, we proceeded to commissioning, which was followed by the first plasma operation.

3.1. Vacuum pumping

The vacuum pumping system consists of one pumping unit for the plasma vacuum vessel and one pumping unit for the cryostat for thermal isolation. Manifolds with diameters of 1.2 m, as shown in Fig. 1, and 0.8 m are connected to the plasma vacuum vessel and to the cryostat, respectively. The pumping unit for the plasma vacuum vessel includes two cryogenic pumps with a pumping speed of 70 m^3/s for water, two turbomolecular pumps with a pumping speed of 5 m^3/s for nitrogen, two compound turbomolecular pumps with a pumping speed of 1.8 m^3/s for nitrogen, one

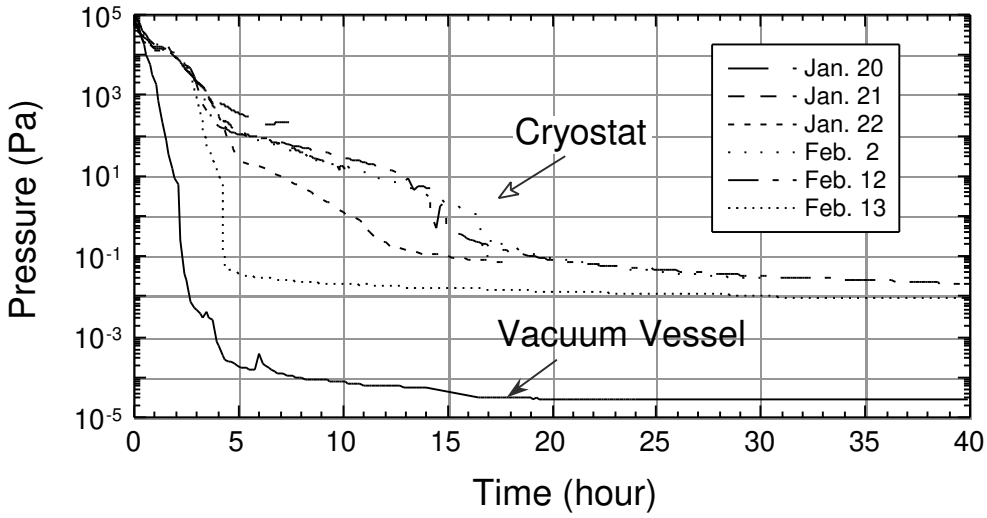

Figure 3. Cryostat and plasma vacuum vessel pressures as a function of time.

mechanical booster pump with a pumping speed of 1630 m^3/h and four rotary pumps with a pumping speed of 85 m^3/h. The pumping unit for the cryostat is two cryogenic pumps with a pumping speed of 25 m^3/s for water, two compound turbomolecular pumps with a pumping speed of 5.5 m^3/s for nitrogen, one mechanical booster pump with a pumping speed of 1630 m^3/h and two rotary pumps with a pumping speed of 85 m^3/h. Two oil rotary pumps with a pumping speed of 900 m^3/h are used for first roughing.

The vacuum test of the cryostat began on 20 January 1998. The cryostat, which has a volume of 580 m^3 and an extended surface of about 70 km^2, was evacuated by introducing dry nitrogen for water vapour purge intermittently at 20-200 Pa up to 0.1 MPa. As shown in Fig. 3, we achieved a cryostat pressure of about 0.02 Pa within 3 1/2 days, low enough for the cool down of LHD. The main species of the desorbed gas was found to be water, as expected. During the helium leak test a few small leaks were found in the helium cooling pipes that are located inside the cryostat. These were plugged, and no leak has been left in the cryostat in the range of 10^{-8} Pam^3/s. The vacuum test of the plasma vacuum vessel began on 30 January. The pressure of the plasma vacuum vessel reached 3×10^{-5} Pa within a day, and no leak was found in the plasma vacuum vessel and water cooling pipes in the range of 10^{-9} Pam^3/s. At the end of March, the pressure of the plasma vacuum vessel reached 9×10^{-7} Pa.

3.2. Cool down

We started the main compressors on 9 February 1998, and continued the purifying operation of the cryogenic system until 22 February to remove impurities in the helium gas, such as oxygen, nitrogen and water, to less than 2 ppm. The first cool down of LHD started on 23 February and finished on 22 March. Figure 4 shows the cooling curves of the helical and poloidal coils as well as the date of the transition to the superconducting state, indicated by the voltage drops of the coils at 10 A coil currents. At first the superconducting coils, supporting structures and 80 K shield were

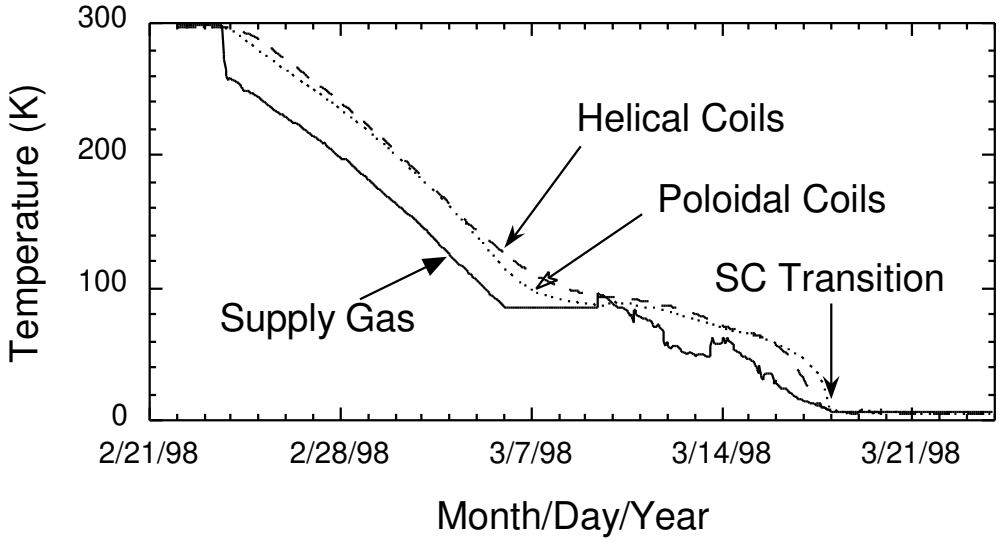

Figure 4. Cool-down curves of helical and poloidal coils.

cooled by helium gas, the temperature of which was controlled by mixing cold and warm gases in order to keep the temperature distribution in the coils and supporting structures less than 50 K. Thus this temperature distribution determined the cooling rate. Below 85 K, seven turboexpanders were put into operation. The helical coils, poloidal coils and superconducting buslines have turned into superconductors since 18 March, when the supply gas temperature was 8.5 K and the coil outlet gas temperature was 9.0 K.

3.3. Field generation

After all the coils were completely cooled down and liquid helium was stored sufficiently, the first excitation test of the superconducting coils was conducted. Through the process of debugging the control program and adjusting the feedback gain of current control in low currents, the coils were successfully excited up to 1.5 T without abnormal heat generation in the coils on 27 March. The accuracy of current control did not reach the target value in the initial operation, but it was improved at the end of the first plasma experimental campaign [20].

4. Initial plasma experiments

4.1. Magnetic flux mapping

Magnetic flux mapping was done under steady state conditions at reduced magnetic fields ranging up to 0.25 T, using the fluorescence method. In the measurements, an electron gun with a LaB6 cathode and a fluorescent mesh were used. The diameter of the electron beam was limited to less than 3 mm. The fluorescent mesh of 1 m $\times$ 2 m was located at the toroidal plane, the cross-section of which is elongated vertically. The magnetic surfaces were measured by taking pictures of

the beam images on the fluorescent mesh while changing the radial position of the electron gun. The pictures were taken with an intensified charge coupled device (CCD) camera, which was aligned in parallel with the tangential port for the NBI.

Clear pictures of the magnetic surfaces were obtained, as shown in Fig. 5(a). It is quite obvious that there are closed, nested magnetic surfaces, in good agreement with the theoretical calculation, as can be seen in Fig. 5(b). Figure 5(a) also shows the existence of a clear m/n = 1/1 island. This island is considered to be formed by the terrestrial magnetism, because the magnetic field was low when the mapping was performed. In Fig. 5(b), the magnetic surfaces were calculated taking into account the terrestrial magnetism and demonstrating that the m/n = 1/1 and 2/1 islands can indeed be formed by the terrestrial magnetism at this low magnetic field. The calculated poloidal phases and maximum widths of the islands are found to agree well with those of the experimental results. The maximum width of the m/n = 1/1 island was reduced by a factor of about 1.3 when the mapping was performed at B_t = 0.25 T compared with that at B_t = 0.0875 T. Even at this stage of the magnetic flux mapping studies, it is suggested that the accuracy in LHD's helical and poloidal coils and their alignment is better than the value required.

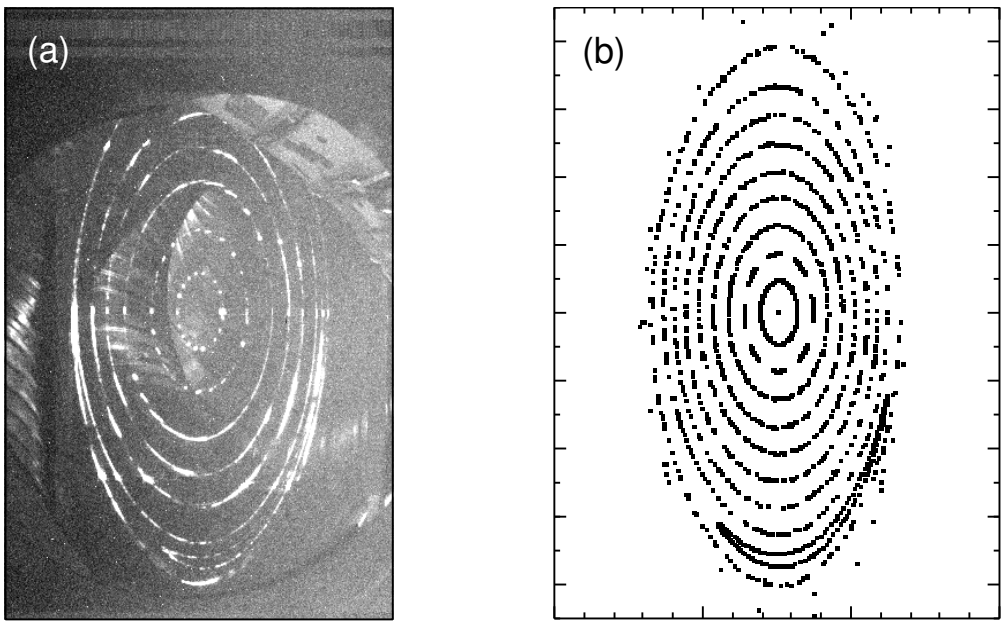

Figure 5. (a) Measured and (b) calculated magnetic surfaces at B_t = 0.0875 T. In the calculation, the terrestrial magnetism is taken into account.

4.2. Wall conditioning

Hydrogen discharge cleaning of the plasma vacuum vessel was done with the standard magnetic configuration of 0.0875 T using the 2.45 GHz ECR system with a power of 10 kW. Then the first plasma was produced with ECH of 150 kW on 31 March. Baking the plasma vacuum vessel at temperatures of around 95℃ was performed after the first plasma, and hydrogen and helium ECR

discharge cleaning with a power of 5 kW was performed before and after Ti gettering, respectively. The main desorbed gases were hydrogen, carbon monoxide and water. To enhance wall conditioning, the toroidally distributed Ti gettering was done once or twice a day, which covers 20 - 30% of the plasma facing wall surface.

Figure 6 shows the evolution of the plasma stored energy W_p and evacuated molecular layers as a function of shot number in the first campaign, demonstrating that W_p increased remarkably after the impurity gas was evacuated. The total amount of oxygen is about 100 molecular layers, i.e. about 50 g. At the end of the first campaign, W_P reached about 15 kJ. The electron temperature T_e exceeded 1.3 keV and $\bar{n}_e$ was of the order of 5×10^{18} m^{-3}.

In the second campaign, after the plasma vacuum vessel was baked for 240 h, helium glow discharge cleaning with a power of 5 kW, partly combined with helium ECR discharge cleaning, was carried out, including the conditioning of the NBI ports. This resulted in good wall conditioning, and more or less the same result as in the first campaign was obtained. After high power NBI operation, glow discharge cleaning was effective in improving the wall condition.

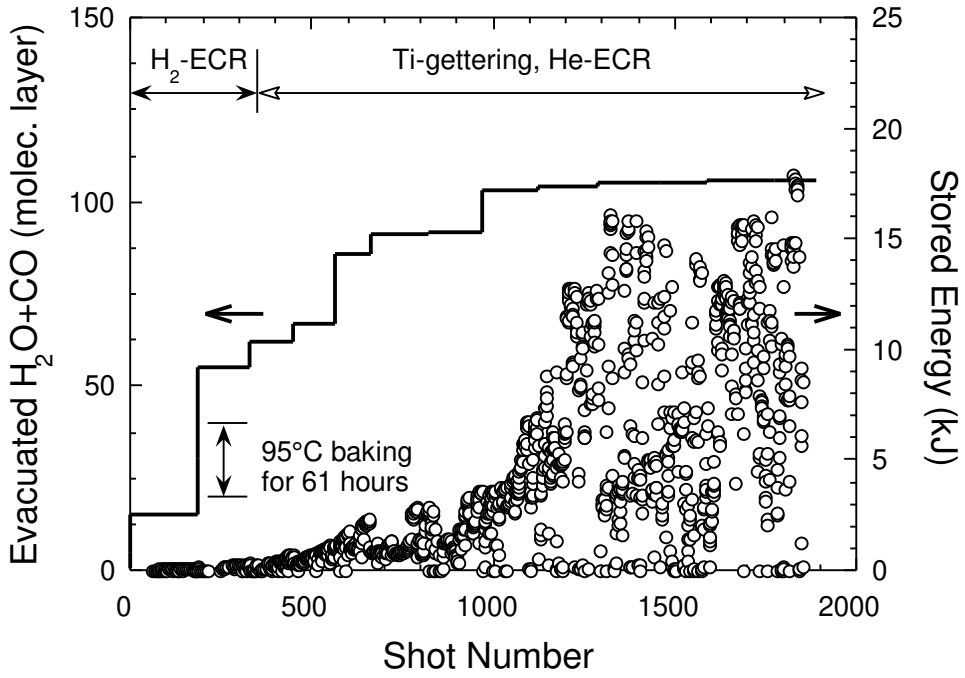

Figure 6. Total amount of evacuated impurity gases and stored energy as a function of shot number in the first campaign.

4.3. ECH plasma

In the first campaign, which continued to 13 May 1998, plasmas were produced by two gyrotrons. The total input power was 0.35 MW for a pulse duration of 0.25-0.5 s. It was found that an abrupt increase of $\bar{n}_e$ during startup of the plasma discharge is accompanied by the expansion of

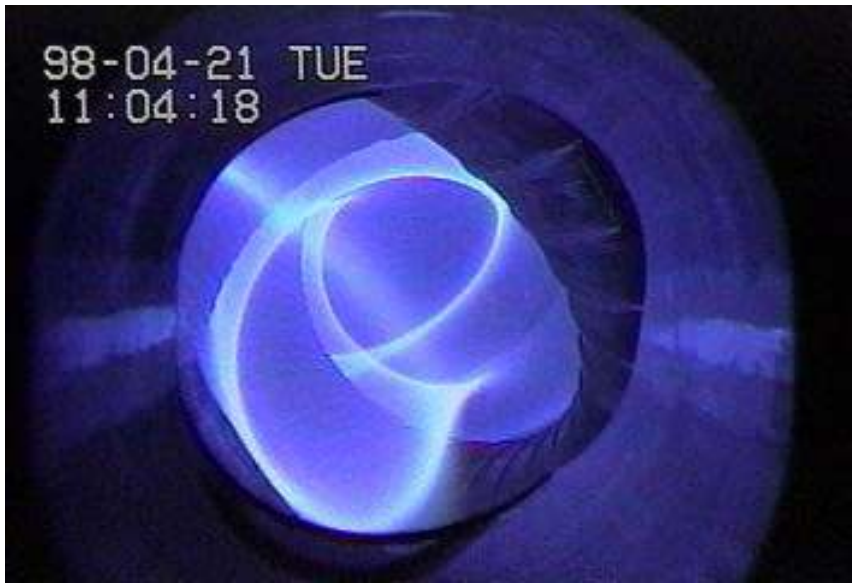

Figure 7. TV image of the LHD plasma, which is well expanded.

the plasma volume. At first the plasma is produced only around the resonance point, located at the plasma centre, because the elliptical Gaussian beam of ECH is focused at the resonance point on the equatorial plane. Then the plasma volume becomes large. Figure 7 shows a TV image of the plasma, which is well expanded and wrapped in a luminous layer. The time evolution of the plasma radius can be obtained by measuring the position of this luminous layer. The TV image also demonstrated that the plasma radius is changed by the balance of the input power and the total amount of gases puffed and released from the plasma vacuum wall. Diverted plasma flux profiles have been measured with a 30 channel array of Langmuir probes located outside the X point. Particle fluxes with high T_e of 20 eV, which are measured as the ion saturation currents, are detected at the same time that the luminous layer reaches the divertor region indicate good agreement with the time evolution of the TV image of the plasma. Furthermore, a well defined profile of the ion saturation current with a half-maximum width of less than 10 mm was observed. The peak positions agree well with the results of the magnetic field calculations, to within $\pm$5 mm.

The plasma parameters achieved in the first campaign are summarized as follows: (1) T_e of 1.3 keV and $\overline{n}_e$ of 3×10^{18} m^{-3} at ECH power of 270 kW; (2) $\overline{n}_e$ of 1.3×10^{19} m^{-3} at ECH power of 80 kW; (3) energy confinement time τ_E of up to 0.25 s at $\overline{n}_e$ of 6×10^{18} m^{-3} and ECH power of 70 kW. Although the experiment was usually performed at a magnetic axis position R_{ax} of 3.75 m, data were also taken at R_{ax} = 3.9 m. The comparison between these data indicates that better confinement is achieved at R_{ax} =3.75 m than at R_{ax} =3.9 m, as expected from the calculation of particle orbits.

An LID experiment was performed using only the LID magnetic configuration, where an m/n = 1/1 island is generated by the 20 LID coils, to study the effect of the LID magnetic configuration on the ECH plasma. In the usual LID experiment, the outward heat and particle fluxes crossing the island separatrix flow along the field lines to the back of the island, where target plates are placed on a divertor head [5, 6]. The particles recycled there are pumped, and hence the geometrical shapes

of the divertor head and pumping duct should be designed to form a closed divertor configuration with a high pumping efficiency [5]. The divertor head was, however, not used in the first campaign, because it had not yet been constructed. We found that the plasma parameters change significantly when the plasma is not fully expanded. In this case, the radiation power, measured with a bolometer, and the O V and C III radiation intensities decrease significantly in the LID magnetic configuration, while $\bar{n}_e$ decreases slightly. The stored energy W_p measured by a diamagnetic loop increases significantly, suggesting improved confinement. However, the plasma parameters change little when the plasma is fully expanded. A detailed analysis is under way in preparation for the next LID experiment.

Quasi-steady-state operation with a duration of 140 s was attained at the end of the first campaign. An ECH pulse train of 80 kW/1 Hz/10% duty was injected into the plasma. Despite the fact that the power input is not truly continuous, an AC mode of operation was achieved. During this AC plasma operation, impurities such as O V and C III were also observed to keep track of the plasma density evolution.

4.4. Auxiliary heating plasmas

In the second campaign, two 84 GHz gyrotrons and one 82.6 GHz gyrotron are used for producing a target plasma for NBI. The total input power of ECH is around 0.42 MW for a pulse duration of 0.25-0.4 s. In the ECH phase, $\bar{n}_e$ and W_p are measured to be 1.7×10^{19} m^{-3} and about 36

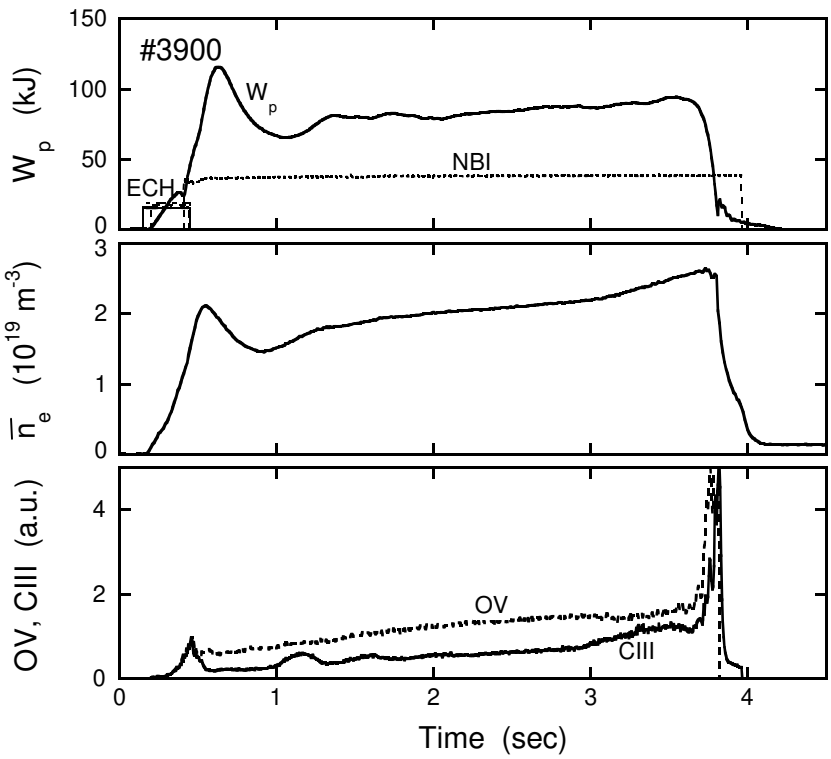

Figure 8. Time evolution of stored energy W_p, averaged electron density $\bar{n}_e$, OV radiation intensity and CIII radiation intensity.

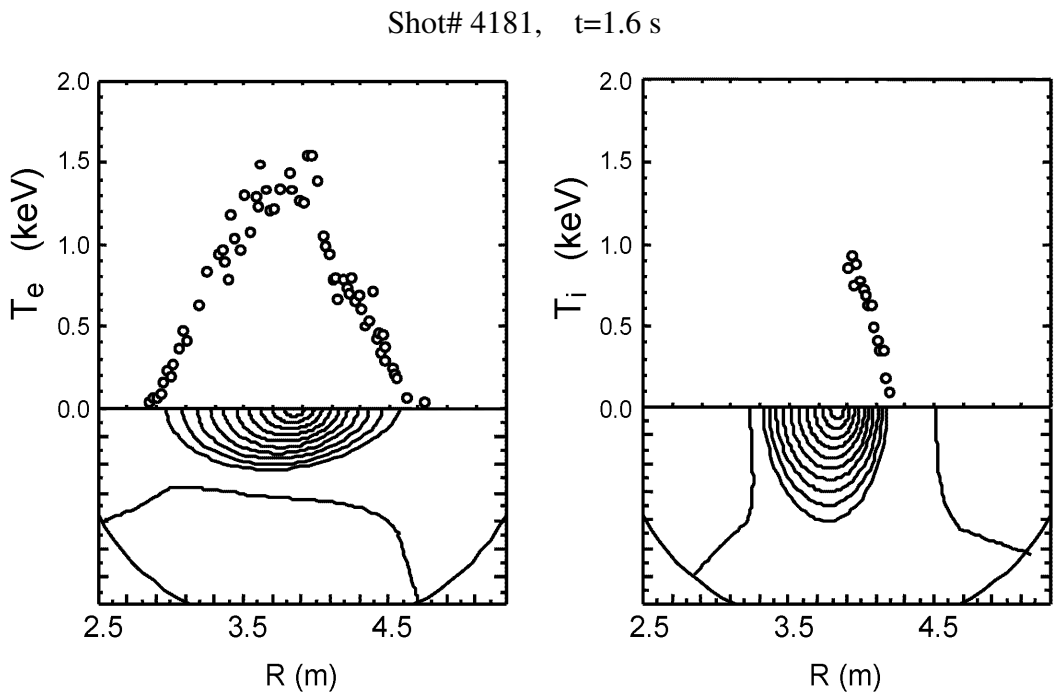

Figure 9. Radial profiles of electron temperature T_e and ion temperature T_i.

kJ. The ion sources for NBI are optimized for a low energy of 100 keV, considering that the target plasma density is low in the case of 1.5 T operation. In this case, the maximum injecting beam power is limited to 4-5 MW for 1 s.

In the presence of NBI with a duration of less than 0.5 s, $\overline{n}_e$ in hydrogen puffing discharges is found to decrease significantly and the diverted plasma flux increases during this pumping phase. LHD employs metal walls, i.e. stainless steel walls, and has no limiter. Thus it is considered that the metal walls strongly pump the hydrogen plasma and that the global recycling coefficient in LHD is less than unity. The increase in NBI power results in a shorter decay time of the density drop. The hydrogen pellet injection experiment, performed for the purpose of fuelling, also shows a large decrease in $\overline{n}_e$ after its sudden increase at the instant the pellet is injected. Because the wall is considered to be saturable, the investigation of discharges longer than 0.5 s has just started, with control of the gas puffing. By contrast, in helium discharges, where helium gas puffing is performed while the beam species is hydrogen, the wall pumping phenomenon is much milder, and $\overline{n}_e$ can be kept almost constant during discharges with a duration of less than a few seconds.

The time evolution of plasma parameters is shown in Fig. 8, for the helium puffing discharge. The maximum duration of the discharge is about 10 s at this stage. The profiles of T_e and of ion temperature T_i are shown in Fig. 9. It should be noted that T_i at the outermost flux surface reaches 300 eV, suggesting the feasibility of high temperature divertor operation, where a divertor plasma with a temperature of a few kiloelectronvolts is produced, leading to a significant energy confinement improvement [21]. The plasma parameters attained in the hydrogen gas puffing are summarized in Table 3; $n\tau T$ is 8×10^{18} keVm^{-3}s and $<\beta>$ is 0.7%. These are about one tenth of the

Table 3. Plasma parameters attained in experiments

	T_e (keV)	T_i (keV)	τ_E (sec)	P_{abs} (MW)	$\bar{n}_e$ (10^{19} m^{-3})
High Temperature	1.5	1.1	0.11	1.6	1.5
	-	1.4	-	-	0.4
High Confinement	0.8	-	0.17	1.3	5.0
Fusion Triple Product = 8×10^{18} keV m^{-3} sec					
Maximum Density					
6.3×10^{19} m^{-3} (Helium gas puff)					
6.0×10^{19} m^{-3} (Hydrogen pellet)					
Maximum Stored Energy					
W_p = 0.22 MJ					
$\langle\beta\rangle$ = 0.7 % with 3 MW Port-through					

goal values. The maximum T_i is 1.4 keV at low $\bar{n}_e$ of less than 4×10^{18} m^{-3}.

Figure 10 shows the energy confinement time τ_E and the ISS95 scaling law, $\tau_E^{ISS95} = 0.079\, a^{2.21} R^{0.65} B_t^{0.83} \bar{n}_e^{0.51} P_{abs}^{-0.59} (\iota/2\pi)_{2/3}^{0.4}$, where P_{abs} and ι are the total absorbed power and the rotational transform, respectively [22]. The energy confinement time τ_E was estimated on the basis of W_p measured by the diamagnetic loops. The response of the diamagnetic loops has been calculated by a

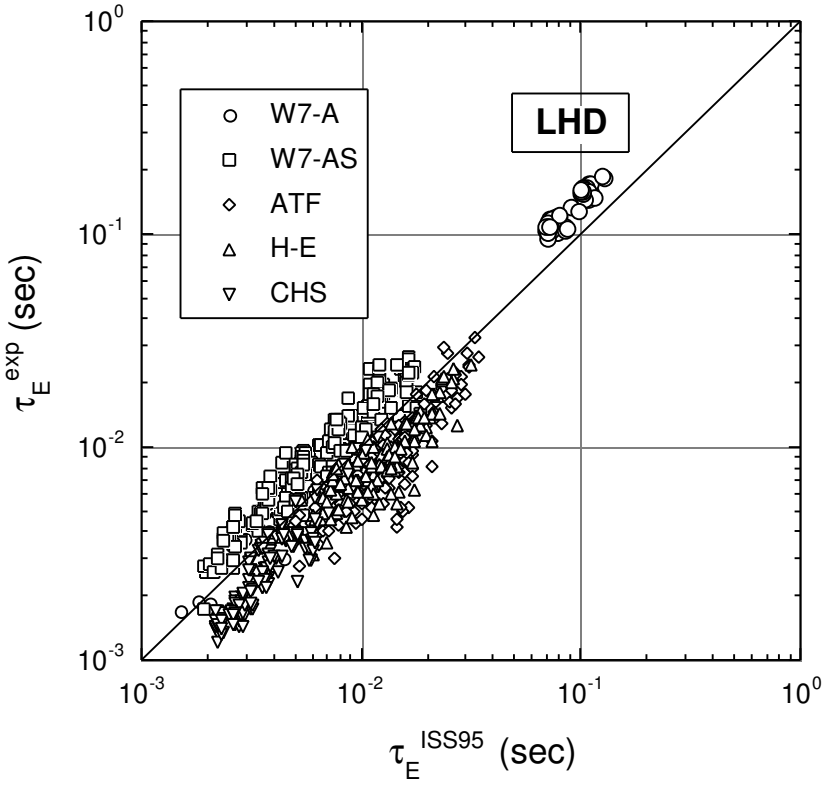

Figure 10. Energy confinement time data vs. the ISS95 scaling law.

3-D magnetic field analysis with 3-D finite-β equilibrium. The NBI deposition profiles were evaluated using a Monte Carlo simulation code, MCNBI [23] and the ECH deposition power was derived from the water load measurement considering losses due to mirrors and bends in the wave guides. All data in Fig. 10 were taken at R_{ax} = 3.75 m during hydrogen gas puffing. We found that LHD's τ_E is clearly longer than those of the existing helical devices by about one order of magnitude and that τ_E is longer than τ_E^{ISS95}, representing better energy confinement than the ISS95 scaling law. Details on physics results are presented elsewhere [24].

The ICRF heating experiment also will start in the second campaign. One pair of fast wave antenna was installed for electron/ion heating. The expected loading power is 1 MW for 1 s, which will be increased up to 2 MW for 10 s or 0.5 MW at steady state.

5. Future plans

Figure 11 shows the near term schedule of LHD experiments. The excitation test to the rated field of 3 T is planned during this conference. From the third experimental campaign, experiments will be conducted at B_t = 3 T, with the heating power being increased gradually. The ECH power is planned to range from 3 to 10 MW. The beam energy of NBI will be increased up to 180 keV and the injection power up to 10 MW. For full power operation at a heating power of 15 MW, the ion sources will be modified to reduce the electron component. For the ICRF heating experiments, a folded wave guide antenna will be installed before the next campaign for ion Bernstein heating, by which plasma production can be done independently of the magnetic field. The expected loading

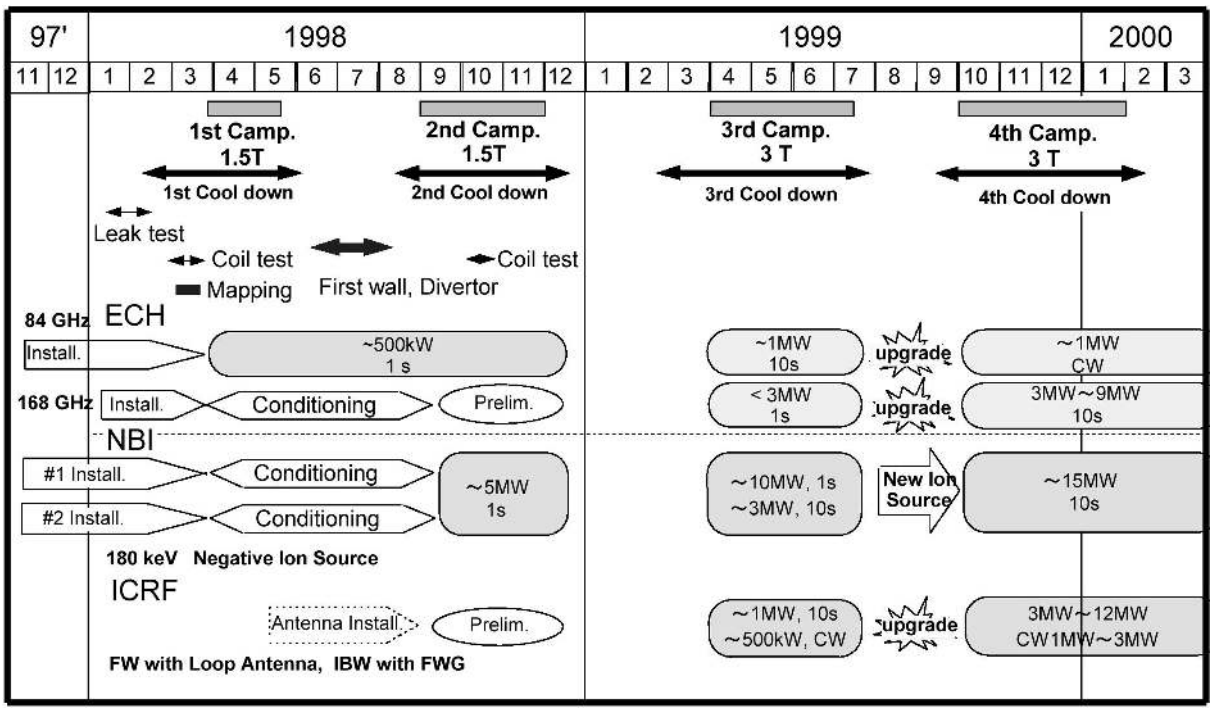

Figure 11. Near-term scheme of LHD experiments.

power is 1 MW for 1 s, which will be increased up to 2 MW for 10 s. In the future we plan to install more antennas to increase the loading power up to 12 MW for 10 s or 3 MW at steady state.

For edge plasma control, the LID has been tested in 1998-1999, and the divertor head will be installed in 1999 or 2000. The helical divertor will be examined in one pitch of the helical structure. Steady state operation at the 1 MW level is being tried first, with gradual increase up to 3 MW, in parallel with the development of the heat removal method in 1998-2001 [25].

In the upgrade phase, i.e. Phase II, the magnetic field will be increased to 4 T by 1.8 K operation of the helical coil. The full helical divertor equipped with baffle plates, with which closed divertor operation is possible, will be installed, and D beams will be injected into D plasmas.

6. Summary

After challenging technology R&D over a period of eight years, the construction of LHD has recently been completed. The first evacuation and cooldown were performed, and the helical coils and poloidal coils successfully became superconductive. Auxiliary heating experiments with NBI of 3 MW have achieved an electron temperature of 1.5 keV and an ion temperature of 1.1 keV, with an averaged electron density of 1.5×10^{19} m^{-3} at a magnetic field of 1.5 T. The maximum ion temperature is 1.4 keV. The maximum stored energy has reached 0.22 MJ, which corresponds to $\langle\beta\rangle = 0.7\%$. The energy confinement time has shown some enhancement over the present scaling law, which was derived from existing medium size helical devices, and the maximum value has exceeded 0.25 s.

From the third campaign, experiments will be conducted at a magnetic field of 3 T with the heating power increased gradually. We are aiming at achieving improved confinement in LHD like the H mode in tokamaks.

The goals of the LHD experiments are to understand the physics of steady state currentless plasmas and to demonstrate the feasibility of heliotrons as power reactors. In order that these goals are achieved, worldwide collaboration and participation in the LHD experiments are invited.

Acknowledgements

Fusion research is based on the integration of plasma physics, fusion science and reactor engineering. The LHD project has been supported by many co-workers in these fields from universities, institutes and industries in Japan and throughout the world. We would like to thank all of these people for their contributions.

References

[1] IIYOSHI, A., et al., Fusion Technol. **17** (1990) 169.
[2] MOTOJIMA, O., et al., in Plasma Physics and Controlled Nuclear Fusion Research 1990 (Proc. 13th Int. Conf. Washington DC, 1990), Vol. 3, IAEA, Vienna (1991) 513.
[3] YAMAZAKI, K., et al., ibid., Vol. 2, p. 709.
[4] FUJIWARA, M., et al., Plasma Phys. Control. Fusion **39** (1997) A261.
[5] KOMORI, A., et al., in Plasma Physics and Controlled Nuclear Fusion Research 1994 (Proc. 15th Int. Conf. Seville, 1994), Vol. 2, IAEA, Vienna (1995) 773.
[6] KOMORI, A., et al., in Fusion Energy 1996 (Proc. 16th Int. Conf. Montreal, 1996), Vol. 2, IAEA, Vienna (1997) 3.
[7] MOTOJIMA, O., et al., Nucl. Fusion **39** (1999).
[8] MITO, T., et al., Fusion Eng. Des. **10** (1993) 233.
[9] YANAGI, N., et al., Adv. Cryog. Eng. **40** (1994) 459.
[10] TAKAHATA, K., et al., Fusion Eng. Des. **20** (1993) 161.
[11] YAMADA, S., et al., IEEE Trans. Magn. **32** (1996) 2422.
[12] SENBA, T., et al., in Fusion Technology 1994 (Proc. 18th Int. Conf. Karlsruhe, 1994), Vol. 2, Elsevier, Amsterdam (1995) 905.
[13] NISHIMURA, A., et al., in Fusion Technology 1998 (Proc. Symp. Marseilles, 1998), Vol. 1, Centre d'etudes de Cadarache, Saint-Paul-lez-Durance (1998) 869.
[14] CHIKARAISHI, H., et al., in Proc. Power Conversion Conf. Nagaoka, 1997, IEE Japan, Tokyo (1997) 747.
[15] MITO, T., et al., Adv. Cryog. Eng. **43** (1998) 589.
[16] SUZUKI, H., et al., Trans. Fusion Technol. **27** (1995) 523.
[17] SUZUKI, H., et al., J. Plasma Fusion Res. **1** (1998) 402.
[18] FUJITA, J., Fusion Eng. Des. **34&35** (1997) 11.
[19] SATOW, T., et al., Proc. ICEC-16/ICMC-1997, Kitakyusyu, Elsevier, Oxford (1997) 735.
[20] CHIKARAISHI, H., et al., in Fusion Technology 1998 (Proc. Symp. Marseilles, 1998), Vol. 1, Centre d'etudes de Cadarache, Saint-Paul-lez-Durance (1998) 759.
[21] OHYABU, N., et al., Nucl. Fusion **34** (1994) 387.
[22] STROTH, U., et al., Nucl. Fusion **36** (1996) 1063.
[23] MURAKAMI, S., et al., Trans. Fusion Technol. **27** (1995) 256.
[24] FUJIWARA, M., et al., Nucl. Fusion **39** (1999).
[25] NODA, N., et al., J. Plasma Fusion Res. **1** (1998) 130.